

Spherical shock-ignition experiments with the 40 + 20-beam configuration on OMEGA

W. Theobald, R. Nora, M. Lafon, A. Casner, X. Ribeyre et al.

Citation: *Phys. Plasmas* **19**, 102706 (2012); doi: 10.1063/1.4763556

View online: <http://dx.doi.org/10.1063/1.4763556>

View Table of Contents: <http://pop.aip.org/resource/1/PHPAEN/v19/i10>

Published by the [American Institute of Physics](#).

Related Articles

Observed transition from Richtmyer-Meshkov jet formation through feedout oscillations to Rayleigh-Taylor instability in a laser target

Phys. Plasmas **19**, 102707 (2012)

Driving high-gain shock-ignited inertial confinement fusion targets by green laser light

Phys. Plasmas **19**, 090702 (2012)

Role of shocks and mix caused by capsule defects

Phys. Plasmas **19**, 092703 (2012)

Ion dynamics at supercritical quasi-parallel shocks: Hybrid simulations

Phys. Plasmas **19**, 092108 (2012)

Invited Article: Relation between electric and magnetic field structures and their proton-beam images

Rev. Sci. Instrum. **83**, 101301 (2012)

Additional information on Phys. Plasmas

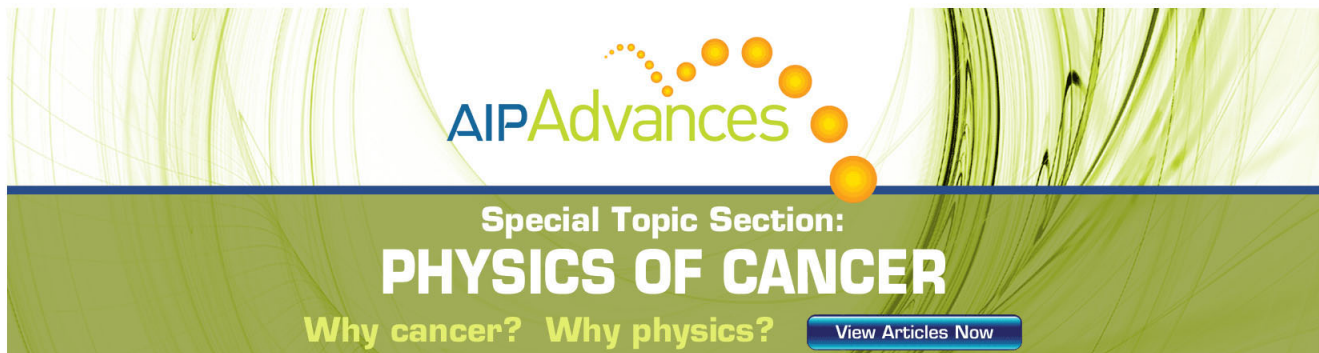
Journal Homepage: <http://pop.aip.org/>

Journal Information: http://pop.aip.org/about/about_the_journal

Top downloads: http://pop.aip.org/features/most_downloaded

Information for Authors: <http://pop.aip.org/authors>

ADVERTISEMENT



AIP Advances

Special Topic Section:
PHYSICS OF CANCER

Why cancer? Why physics? [View Articles Now](#)

Spherical shock-ignition experiments with the 40 + 20-beam configuration on OMEGA

W. Theobald,^{1,a)} R. Nora,^{1,2} M. Lafon,^{1,3} A. Casner,⁴ X. Ribeyre,³ K. S. Anderson,¹ R. Betti,^{1,2} J. A. Delettrez,¹ J. A. Frenje,⁵ V. Yu. Glebov,¹ O. V. Gotchev,¹ M. Hohenberger,¹ S. X. Hu,¹ F. J. Marshall,¹ D. D. Meyerhofer,^{1,2} T. C. Sangster,¹ G. Schurtz,³ W. Seka,¹ V. A. Smalyuk,^{1,6} C. Stoeckl,¹ and B. Yaakobi¹

¹Laboratory for Laser Energetics and Fusion Science Center, University of Rochester, Rochester, New York 14623, USA

²Department of Mechanical Engineering and Physics at the University of Rochester, Rochester, New York 14623, USA

³University of Bordeaux, CEA, CNRS, CELIA (Centre Lasers Intenses et Applications), F-33400 Talence, France

⁴CEA, DAM, DIF, F-91297 Arpajon, France

⁵Massachusetts Institute of Technology, Cambridge, Massachusetts 02139, USA

⁶Lawrence Livermore National Laboratory, Livermore, California 94550, USA

(Received 21 June 2012; accepted 3 October 2012; published online 24 October 2012)

Spherical shock-ignition experiments on OMEGA used a novel beam configuration that separates low-intensity compression beams and high-intensity spike beams. Significant improvements in the performance of plastic-shell, D₂ implosions were observed with repointed beams. The analysis of the coupling of the high-intensity spike beam energy into the imploding capsule indicates that absorbed hot-electron energy contributes to the coupling. The backscattering of laser energy was measured to reach up to 36% at single-beam intensities of $\sim 8 \times 10^{15}$ W/cm². Hard x-ray measurements revealed a relatively low hot-electron temperature of ~ 30 keV independent of intensity and timing. At the highest intensity, stimulated Brillouin scattering occurs near and above the quarter-critical density and the two-plasmon-decay instability is suppressed. © 2012 American Institute of Physics. [<http://dx.doi.org/10.1063/1.4763556>]

I. INTRODUCTION

Shock ignition (SI)¹ is a promising new concept in direct-drive inertial confinement fusion (ICF) that achieves thermonuclear ignition and burn by a strong focusing shock wave in a pre-compressed DT shell.² Shock ignition, as described in Ref. 1, is a two-step scheme designed to enhance the hot-spot compression with respect to the single-step conventional hot-spot ignition.³ SI uses a moderate-intensity assembly laser pulse followed by a subnanosecond high-intensity spike that launches a strong shock wave (the ignitor shock) into the imploding shell. It is important to emphasize that SI does not use a shock wave to directly ignite the dense fuel;⁴ instead, it relies on the collision of the ignitor and the rebound shock waves at the inner shell surface to raise the hot-spot pressure.¹ A non-isobaric fuel assembly with a centrally peaked pressure profile makes SI more energy efficient by lowering the ignition threshold compared to isobaric assemblies.¹ Thick-shell targets containing more fuel can be compressed on a low adiabat with a low implosion velocity, which promises high fusion gains^{1,2,5-7} at moderate laser energies. One-dimensional (1-D) simulations^{7,8} have described igniting SI designs with as low as ~ 300 kJ of total laser energy. The SI requirements for laser pulse shaping are more demanding than in conventional hot-spot-ignition designs but are still within the pulse-shaping capabilities of currently operating laser systems like the National Ignition Facility (NIF).⁹ Proof-of-principle experiments on the NIF were

recently proposed¹⁰ and SI is also considered to be a viable option⁸ for the European direct-drive HiPER project.¹¹

The intensity of the spike pulse is expected to be a few times of 10^{15} W/cm². At these high intensities, parametric plasma instabilities¹² such as stimulated Brillouin scattering (SBS), stimulated Raman scattering (SRS), and the two-plasmon-decay (TPD) instability are of concern in an ignition target design for two reasons: The instabilities generate energetic electrons that might preheat the shell with the consequence of reducing the final core compression and they increase the back-reflection of the laser light from the target, degrading the laser-energy coupling to the capsule. SI designs typically apply lower laser intensity during the main part of the drive than in hot-spot designs, so these issues might be less important during the early compression phase. Strong growth of laser-plasma instabilities and significant transfer of laser energy to hot electrons are expected during the high-intensity ignitor spike. The areal density increases during the implosion and if the range of the hot electrons is less than the shell thickness, the electrons are stopped in the outer regions of the shell and do not considerably increase the adiabat of the inner part of the shell.¹³ The hot electrons might then be advantageous for SI because they improve the shock strength. The effect of hot electrons on a NIF-scale SI target¹³ was modeled in 1-D for a marginal igniting target using a multigroup diffusion model¹⁴ for the hot electrons. The ignition (time) window for shock launching is considerably wider when the effects of moderate-energy hot electrons are included. The simulations¹³ show that a NIF-scale target

^{a)}email: wthe@lle.rochester.edu.

can efficiently stop up to 150-keV electrons that are generated during the spike pulse. Hot electrons can be beneficial for SI as long as their range is shorter than the shell's thickness. Important parameters are, therefore, the hot-electron temperature, the amount of laser energy that is transferred into electrons, and the time of generation.

This paper presents SI experiments on the OMEGA laser¹⁵ that uses a novel beam configuration called the 40 + 20-beam configuration. Preliminary results with this configuration are discussed in Ref. 16. It uses 40 out of the 60 OMEGA beams to implode the target with a low-intensity laser pulse, and the remaining 20 beams are tightly focused to launch a late shock into the imploding shell. Compared to the highly symmetric 60-beam implosions, the irradiation nonuniformity with normal-incidence beams is higher in the 40 + 20 configuration. The implosion performance was also studied with a beam configuration with repointed beams. The experiments demonstrate significant improvement in the implosion performance (higher neutron yield, higher areal density, and rounder core in x-ray images) with repointed beams. Two-dimensional (2-D) hydrodynamic simulations were performed for the repointed beam configuration. A similar concept, using a dedicated group of beams with a low-intensity pulse to implode the capsule and a second group of beams with a short high-intensity pulse for the ignitor shock wave, might be implemented on the NIF.¹⁷ The 40 + 20 configuration makes it possible to study high-intensity coupling on OMEGA and to measure hot-electron production and laser backscattering for intensities that are SI relevant. Previous spherical target SI experiments¹⁸ on OMEGA studied the fuel assembly with 60-beam symmetric implosions. In those experiments, the shock wave was launched by a spike at the end of the pulse on all 60 beams with a maximum intensity of $\sim 7 \times 10^{14}$ W/cm². OMEGA cannot produce the requisite SI intensity with a compression pulse using the symmetric 60-beam configuration on a standard target because it leads to intensities that are too low to study laser-plasma instabilities. Switching to the 40 + 20-beam configuration allows one to use two separate pulse shapes with high-intensity beams tightly focused to reach intensities up to $\sim 8 \times 10^{15}$ W/cm². While the surface-averaged intensity is still rather low ($\sim 9 \times 10^{14}$ W/cm²), the single-beam intensities (SBIs) are sufficiently high to study laser-plasma interactions at shock-ignition-relevant intensities. The objectives of this work are to study the implosion performance in the 40 + 20-beam configuration, the coupling of laser energy from high-intensity beams into a spherically imploding capsule, and the laser-plasma instabilities at SI-relevant laser intensities.

The paper is organized as follows: Sec. II presents the beam configurations, while Sec. III describes the targets, the laser pulse shapes, and the diagnostics. The areal density measurements are discussed in Sec. IV and the neutron measurements in Sec. V. Both sections include 2-D hydrodynamic simulations. The time-resolved hard x-ray and laser backscatter measurements are presented in Secs. VI and VII. The paper is then summarized in Sec. VIII.

II. BEAM CONFIGURATIONS

The OMEGA system is a 60-beam laser that was built for direct-drive experiments operating at the third harmonic

($\lambda = 351$ nm) of the Nd:glass laser wavelength. The 60 beams are symmetrically distributed around the target chamber in a soccer-ball geometry with the beams located at the vertices of hexagons and pentagons. OMEGA consists of three laser legs, each feeding two clusters with ten beams per cluster; leg 1 feeds clusters 1 and 4, leg 2 feeds clusters 2 and 5, and leg 3 feeds clusters 3 and 6. It is possible to use two independent pulse shapes: one pulse shape in one of the legs and the other pulse shape in the other two legs. For SI studies with a spherical target, this opens up the opportunity to use two separate pulse shapes with independent control over the two beam groups. One pulse shape in two legs implodes the capsule and a short high-intensity spike pulse in the third leg drives a late shock. Two different beam-pointing configurations were used; they are designated A and B in the following configurations. The beam pointing and focusing conditions for both configurations are described in detail in the Appendix. Configuration A used clusters 1, 3, 4, and 6 for the drive and clusters 2 and 5 for the spike with all beams pointed to target center. The configuration with this particular choice of clusters resulted in significant target illumination nonuniformity because of the spatial and temporal separation between both beam groups. The pattern of the 40 drive beams is not as regular as in a standard 60-beam implosion and, assuming perfect power balance, the irradiation nonuniformity was calculated to be $\sim 11\%$ root mean-square (rms) variation compared to less than $\sim 1\%$ in a standard 60-beam spherically symmetric case.¹⁹ A beam profile with a super-Gaussian shape given by $I(r_\mu) = I_0 \exp[-(r_\mu/352)^{4.1}]$, (where r_μ is the radius in μm) was assumed in the 40 drive beams. The focal spot for the 40 drive beams is obtained with distributed phase plates,²⁰ and the laser light was smoothed with polarization smoothing.²¹ No smoothing by spectral dispersion (SSD) was used in all of the 40 + 20 shots. In configuration B, clusters 1, 2, 4, and 5 were used for the drive and clusters 3 and 6 for the spike. The irradiation nonuniformity in the 40 drive beams was $\sim 7\%$ rms in this configuration, which was lower than in the previous configuration. It was further improved to $\sim 3\%$ rms by repointing the beams. Most of the 40 drive beams were moved individually, as shown in Fig. 1, with the arrows representing direction and amount of shift for each beam.

Figure 2 shows the intensity variation of the 40 repointed drive beams in (a) an Aitoff presentation and (b) a 3-D rendering. This illumination pattern was calculated from the projection of the OMEGA beams on the target sphere with initial radius that takes into account the 3-D beam positions, the beam repointing, and the energy distribution in super-Gaussian focal spots on the sphere. The initial 3-D illumination was averaged over the azimuthal angle to perform the Legendre-mode analysis, which resulted in the axisymmetric illumination pattern shown in Fig. 2(c). The analysis provides the initial illumination, which was used as input in the 2-D cylindrical symmetric simulations with the radiation-hydrodynamic code CHIC.²² In fact, the laser energy deposition in CHIC was performed with a 3-D ray-tracing method on a 2-D axisymmetric mesh. Of course, 2-D simulations are only an approximation to an inherent 3-D problem, and while the non-uniformity from the 3-D illumination is

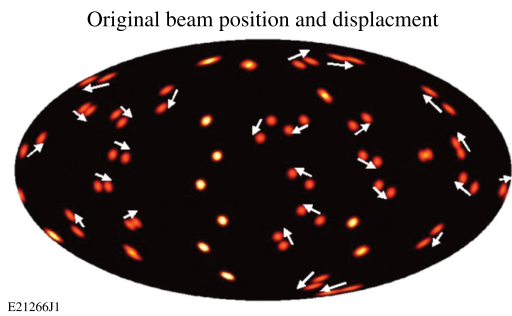


FIG. 1. Aitoff representation of the original beam positions and repositioned positions of the 40 drive beams. Arrows indicate the direction and amount of displacement. Some beams were not moved. The configuration with repositioned beams is referred to with configuration B, while in configuration A, all beams are pointed to target center.

about 3%, the 2-D axisymmetric nonuniformity is less than 1%. The axisymmetric averaging then results in a smoother and more uniform drive in the simulations.²³ A more realistic simulation would require using a 3-D hydro-code. Figure 3 shows the laser-intensity variation of the axisymmetric irradiation pattern versus polar angle and a Legendre-mode analysis, indicating that the modes $\ell=2, 4, 6,$ and 7 are dominant. In addition, a robustness study with respect to power imbalance was performed. A power imbalance of about $\pm 8\%$ on the illumination was assumed. From six random power configurations, the results show that the nonuniformity increases by $\sim 25\%$ to $\sim 3.5\%$ rms. Besides the Legendre mode $\ell=2$, the odd modes 1 and 3 are considerably increased in the presence of power imbalance. Moreover, the maximum of the $\ell=1$ amplitude is equivalent to a target offset of $5 \mu\text{m}$, which further indicates that the 40-beam configuration is sensitive to power imbalance.

To achieve best symmetry in configuration B, a beam repositioning from target center was also performed for the 20 spike beams, as shown in Fig. 4. The 20 beams were moved to the vertices of a dodecahedron pattern. This means that

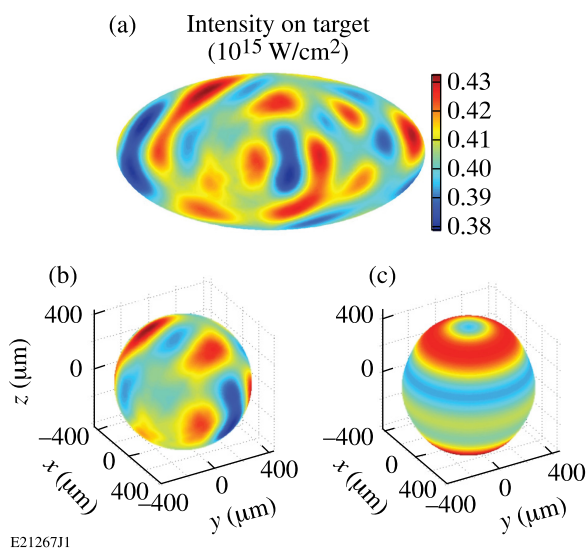


FIG. 2. Intensity variation of 40 repositioned drive beams (configuration B) in (a) an Aitoff representation and (b) in 3-D rendering. (c) The azimuthal averaged intensity distribution was used as input in 2-D cylindrical symmetric hydrodynamic simulations with the code CHIC.²²

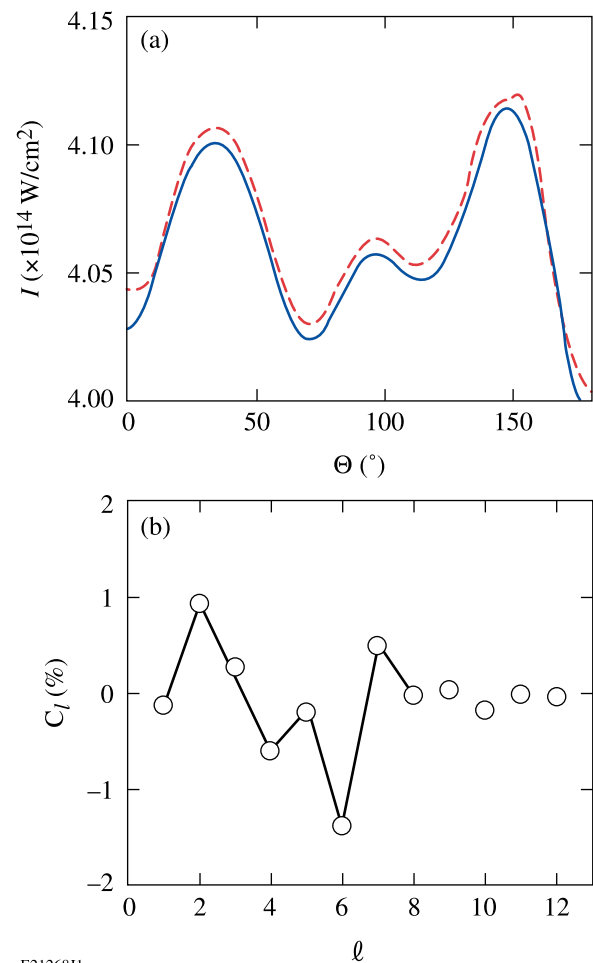


FIG. 3. Laser-intensity variation on target of the axisymmetric irradiation pattern from Fig. 2(c) as a function of (a) polar angle (solid curve—initial irradiation and dashed curve—Legendre polynomial development) and (b) Legendre-mode analysis of the pattern for ℓ below 12. Dominant modes are $\ell=2, 4, 6,$ and 7 .

the beams were repositioned on four rings at the following polar angles: $37.4^\circ, 79.2^\circ, 100.8^\circ,$ and 142.6° . Figure 4 shows that each of the 20 spike beams was moved individually, where the arrows represent the direction and the amount of shift of each beam. Significantly, larger shifts were used in the 20 spike beams.

The single-beam laser intensity of the 20 spike beams on target was controlled by changing the radial beam focal position. The focusing f-number was 6.7 on all 60 beams. It

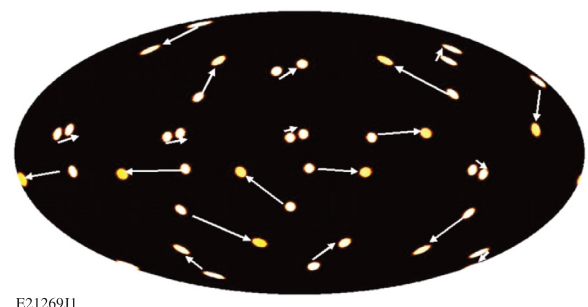


FIG. 4. Aitoff representation of the original beam positions and repositioned positions of the 20 spike beams. Arrows indicate the direction and amount of displacement.

is important to make a clear distinction between the average intensity $\langle I_{\text{spike}} \rangle$ and the SBIs of the spike beams on the capsule surface. The SBI ranges from $I_{\text{spike}} \sim 0.5 \times 10^{15}$ to $\sim 8 \times 10^{15}$ W/cm², while the average intensity on target is not affected as much by the focusing and is $\langle I_{\text{spike}} \rangle \sim 0.5 \times 10^{15}$ W/cm². The average intensity is the relevant quantity to determine the shock strength and the equivalent pressure from the spike beams. The nominal single-beam laser intensity is quoted for vacuum at the location of the critical-density plasma surface at the time when the spike pulse was launched during the implosion as calculated by simulations with the radiation-hydrodynamic codes *LILAC*¹⁴ and *CHIC*. The distance from the critical-density surface to the capsule center was ~ 0.3 mm at 2.7 ns. At best focus, the diameter of the spike beams was estimated with ~ 80 μm , which gave a SBI of $\sim 8 \times 10^{15}$ W/cm². The actual intensity might be different due to plasma effects. Figure 5 shows the intensity pattern of the 20 spike beams for the following spot sizes: ~ 140 μm (SBI $\sim 2.5 \times 10^{15}$ W/cm²), ~ 220 μm (SBI $\sim 1 \times 10^{15}$ W/cm²), and ~ 580 μm (SBI $\sim 0.5 \times 10^{15}$ W/cm²) without the drive beams. The foci of the 20 spike beams did not overlap at the critical-density surface for most lens positions (LPs). Only at the lowest intensity for an ~ 580 - μm spot size, the beams partially overlapped. This created local peak intensities of

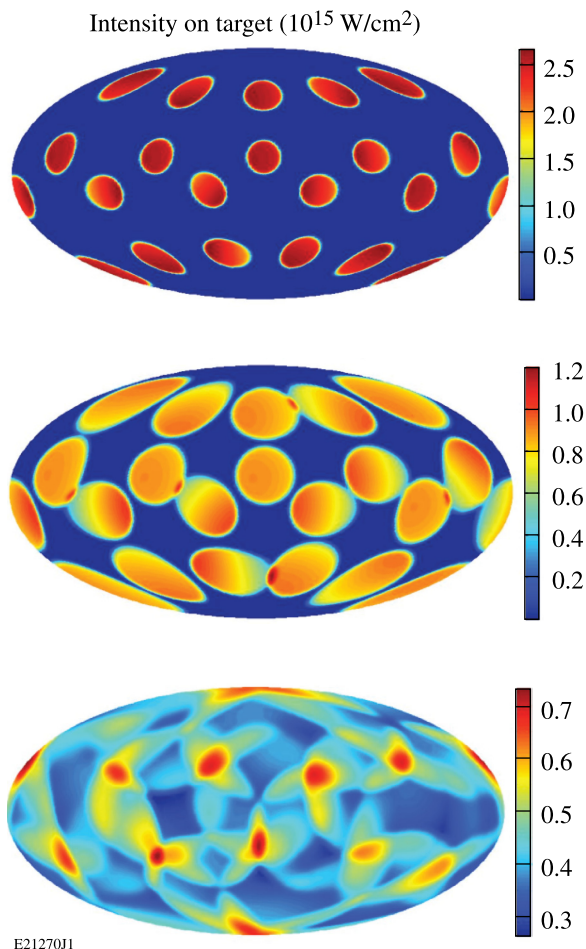


FIG. 5. Intensity variations of the 20 reprinted spike beams (configuration B) in an Aitoff representation. Different lens defocus positions resulted in single-beam spike intensities of $\sim 2.5 \times 10^{15}$ W/cm², $\sim 1 \times 10^{15}$ W/cm², and $\sim 0.5 \times 10^{15}$ W/cm², respectively.

$\sim 0.7 \times 10^{15}$ W/cm² in some regions where several beams overlap. Except for some shots with small-spot phase plates,²⁴ no phase plates were used in the spike beams for most of the shots. The small spot phase plates (E-IDI-300) produced an elliptical focus with a major and minor radius (1/e half width) of 144 ± 2.7 μm and 106 ± 1.4 μm , respectively, and a super-Gaussian beam profile with order $n = 4.3 \pm 0.3$. The intensity distribution in the focus was well characterized. The SBI with small spot phase plates was $\sim 1.1 \times 10^{15}$ W/cm² without drive beams. This is the average intensity of the distribution, which is defined such that half of the beam energy contributes to intensities below the average value and the other half to intensities above the average. The peak intensity is $\sim 3.7 \times 10^{15}$ W/cm² (only 5% of the beam energy exceeds this peak value).

III. TARGETS, PULSE SHAPES, AND DIAGNOSTICS

The targets were ~ 34 - to 36 - μm -thick, ~ 430 - μm -outer-radius, deuterated plastic shells coated outside with a 0.1 - μm layer of aluminum. They were filled with D₂ gas at a pressure of ~ 25 atm. The capsules were imploded on a low adiabat ($\alpha \sim 3$) with a drive pulse shape that is shown for a single beam by the solid curve in Fig. 6. The adiabat α is defined as the ratio of the plasma pressure to the Fermi pressure of a degenerate electron gas. The pulse shape contained ~ 14 kJ of laser energy in 40 beams. Standard 60-beam implosions with the same pulse shape and similar targets, but higher drive energy, are discussed in Refs. 18 and 25. The drive pulse consists of a ~ 100 -ps full-width-at-half-maximum (FWHM) picket pulse preceding a shaped main drive portion with a total duration of 2.7 ns. The 20 spike beams delivered a total energy of ~ 5 kJ on target and used an ~ 600 -ps FWHM square pulse (dashed curve in Fig. 6).

The experimental observables were the spatially resolved x-ray emission from pinhole cameras,²⁶ the neutron yield,²⁷ the neutron-rate,²⁸ the backscattered laser energy,²⁹ the hard x-ray signal,³⁰ and the neutron-rate-averaged areal density (ρR).³¹ The laser light reflected back from the imploded capsule was measured from two adjacent beam ports (a spike-beam and a drive-beam port), which were equipped with a full-aperture backscatter station (FABS).²⁹

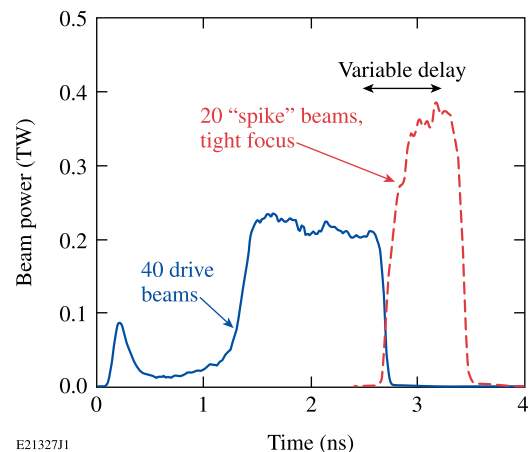


FIG. 6. Single-beam power versus time of the drive-pulse shape (solid) for the 40 beams and the high-intensity pulse (dashed) for the 20 spike beams. Beam delay and spike intensity were varied.

All the spectral measurements were taken on those two FABS ports and not elsewhere. Time-resolved spectra were recorded by two streaked spectrometers covering the wavelength ranges of 351 ± 3 nm for SBS and 450 to 700 nm for SRS. The total backscattered energy in either of these spectral ranges was measured by calorimeters with an uncertainty of $\pm 10\%$. The hard x-ray (HXR) signals were measured with ~ 100 -ps temporal resolution by the HXR detector with four channels measuring x rays >20 , >40 , >60 , and >80 keV, respectively.³⁰ The HXR measurements were used to infer the hot-electron temperature.³⁰

IV. AREAL-DENSITY MEASUREMENTS AND CHIC SIMULATIONS

Close to stagnation of the imploded shell, secondary deuterium fusion reactions in the central hot-spot region produce protons that pass through the dense, cold shell, where they lose energy. The measurement with wedge-range filter spectrometers³¹ provides information about the shell's areal density. This technique makes it possible to accurately reconstruct the proton spectrum and to infer ρR , as discussed in detail in Ref. 31. Figure 7(a) shows two spectra taken at SBI of $\sim 3 \times 10^{15}$ W/cm². Each spectrum represents the average over several spectra from various lines of sight. The solid histogram is from an implosion with configuration A,

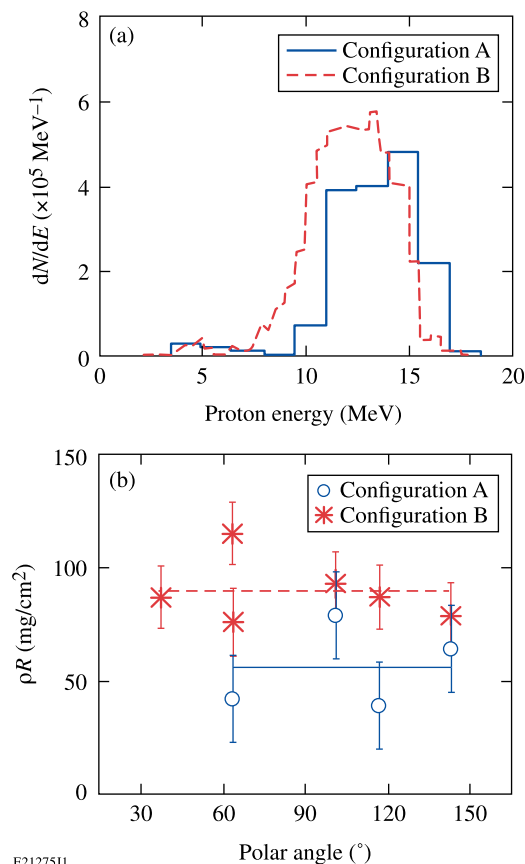


FIG. 7. (a) Secondary proton spectra from an implosion with the beam configuration A (solid) and for the configuration B (dashed) under similar conditions with SBI $\sim 3 \times 10^{15}$ W/cm² and spike onset at ~ 2.3 ns. A lower proton energy spectrum indicates higher areal density. (b) Corresponding neutron-rate-averaged areal densities from different lines of sight are plotted versus the target chamber polar angle.

and the dashed histogram is from configuration B. Lower proton energy indicates a higher ρR . The corresponding ρR from the different lines of sight is plotted versus the target chamber polar angle in Fig. 7(b) with the cross and circle symbols. The corresponding lines represent the average value. The ρR is almost a factor of 2 higher with configuration B, showing that repointing the beams significantly improved the implosion performance. Areal density ρR varies with observation direction, indicating considerable modulation in areal density, which is primarily due to illumination nonuniformities.

Two-dimensional simulations with the code CHIC studied the density and temperature modulations of the imploded capsule at stagnation for configuration B [see Fig. 8(a)]. Figure 8(b) shows simulated (curves) and measured (circles) areal density as a function of the polar angle. The black solid curve is from the 2-D simulation while the dashed line is from a 1-D simulation. The squares mark the 2-D-simulated values at those polar angles used in the measurement. The dotted line is the averaged experimental value. Note that the simulation values are higher because they represent ρR at peak neutron production, while the experimental values are temporally averaged over the neutron-production rate.

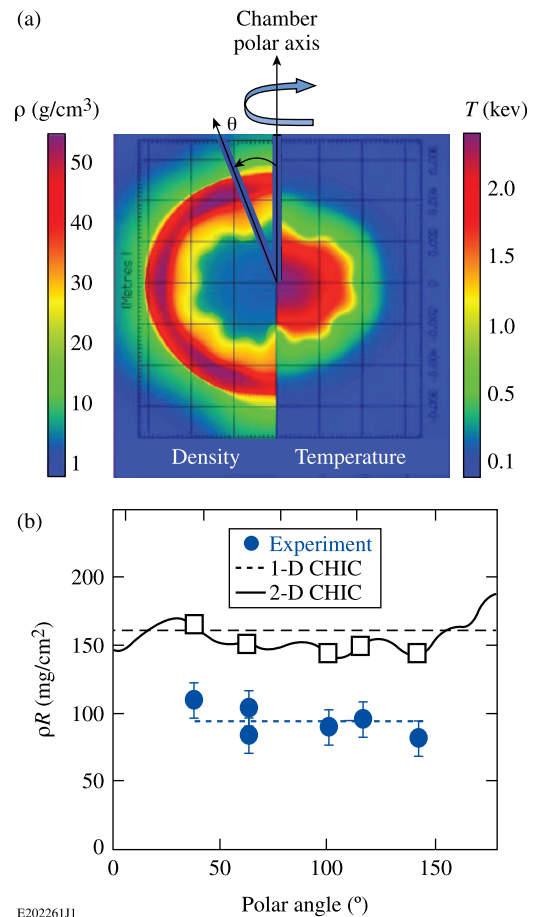


FIG. 8. Two-dimensional (2-D) CHIC²² simulations show significant modulations in the compressed shell. (a) Simulated density and temperature map of a 40 + 20-beam implosion close to stagnation. (b) Simulated (solid and dashed curves, squares) and measured areal density (circles, dotted line) as functions of the polar angle. The SBI was $\sim 3 \times 10^{15}$ W/cm² and spike onset was at ~ 2.6 ns.

The ρR was measured for various onsets of the spike beams with respect to the start of the drive pulse and various SBI. The spike onset was varied from 2.1 to 2.8 ns (see Fig. 6). Figure 9 shows the measured angular-averaged ρR . The symbols represent 40 + 20 implosions, and the line in Fig. 9(b) represents a 40-beam implosion with no spike and ~ 14 kJ of energy. In configuration A [Fig. 9(a)], the proton yield from implosions with only 40 beams was too low to provide a ρR measurement. The ρR values are consistently higher in configuration B [see Fig. 9(b)], showing improved implosion performance. For $\text{SBI} \geq 1.5 \times 10^{15} \text{ W/cm}^2$, there is a tendency of lower ρR for early spike onset. The lower ρR is correlated with a higher hard x-ray signal [see Fig. 9(c)], which could indicate preheating by hot electrons.

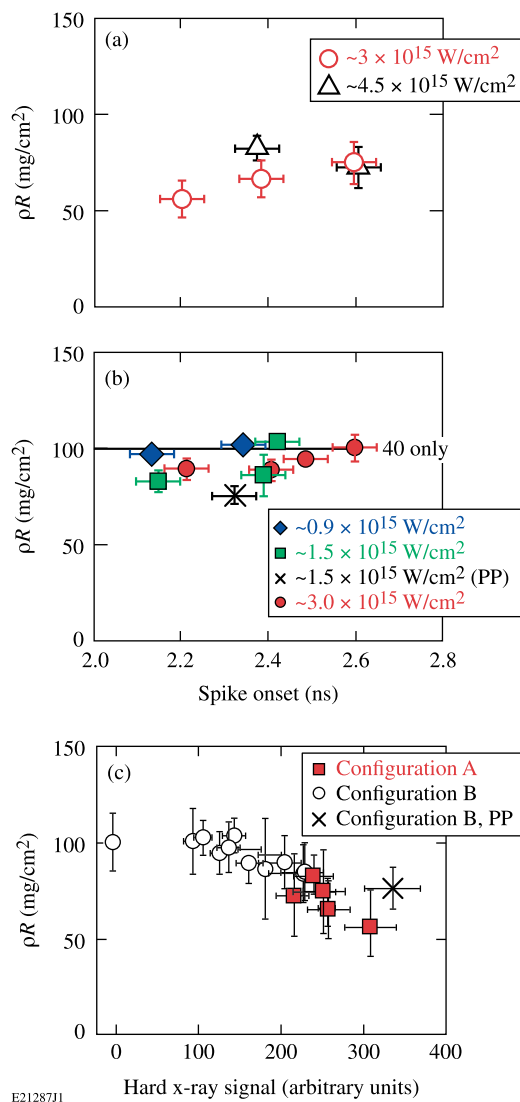


FIG. 9. Measured areal densities from 40 + 20 implosions for (a) configuration A, (b) for configuration B, and (c) for both configurations versus the measured hard x-ray signal. The solid line in (b) represents the measured areal density of a 40-beam implosion. The spike onset and SBI were varied. The SBI given here is the sum of the spike and drive intensity. The solid squares and open circles in (c) represent the measurements in configurations A and B, respectively, and the cross represents the measurement with phase plates in the spike beams in configuration B.

V. NEUTRON MEASUREMENTS AND CHIC SIMULATIONS

Figure 10 shows the measured neutron yield for beam configuration A for various spike-onset times and single-beam intensities. A maximum yield of $\sim 3.5 \times 10^9$ was measured for the shortest time delay. Two reference implosions with only the 40 drive beams produced neutron yields of 1.4×10^8 and 3.7×10^8 ; the solid line in Fig. 10 represents the average of those yields. The low yield of the 40-beam implosion is caused by the large illumination nonuniformity in configuration A, which was also seen in a strongly perturbed core in x-ray pinhole camera images. The x-ray images²⁶ from two different views are shown in Fig. 11(a). The recorded x-ray emission is from the 2- to 7-keV range and comes from the outer shell region, the target stalk, and

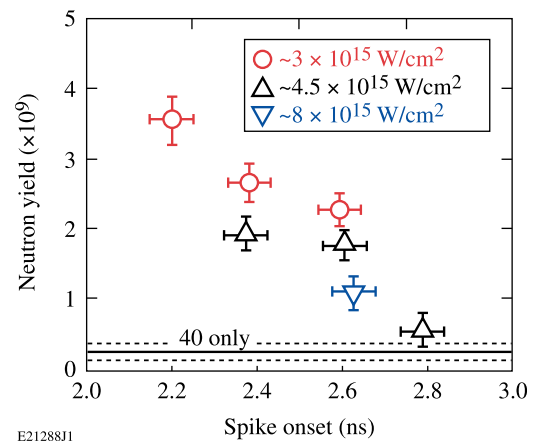


FIG. 10. Measured neutron yield for various spike onset times and SBI for configuration A.

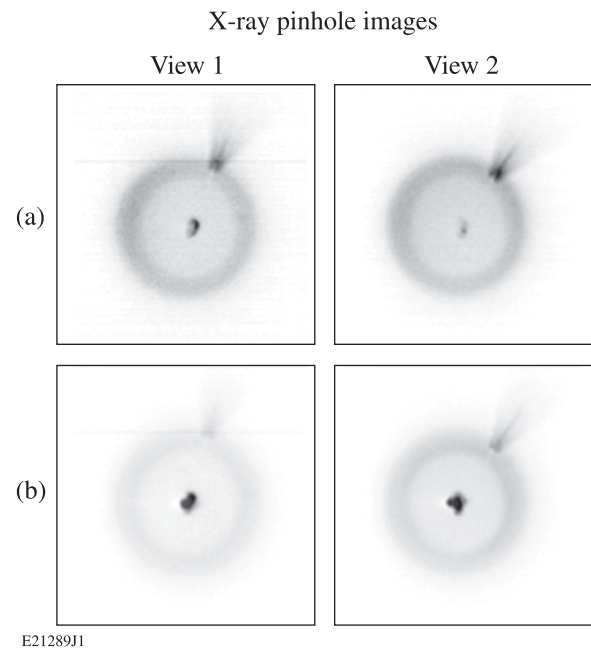


FIG. 11. Measured time-integrated x-ray pinhole images for configuration A. Two views from different directions are shown in each row. (a) The top row represents a 40-beam implosion and (b) the lower row a 40 + 20 implosion. The V-shaped feature in the top right is the emission from the target stalk.

the core region. Adding the spike beams mitigated the non-uniformities, leading to less core distortions [Fig. 11(b)] and a $\sim 14 \times$ increased neutron yield for the earliest spike onset. This shows that a significant amount of the energy from the high-intensity beams was coupled into the capsule. The large illumination nonuniformity in configuration A was partially mitigated by the spike beams, which led to the recovery of the neutron yield. At high intensities, the experimental yield may be affected by a high plasma reflectivity (see Sec. VII), which lowers the coupling efficiency. With later spike onset, there was less temporal overlap between drive and spike pulse and a lower neutron signal was measured. Drive and spike pulse were completely separated at 2.8 ns, which is when the lowest neutron yield was measured. For configuration A, neutron yields are strongly affected by 3-D effects in a highly perturbed core.

Similar implosions were performed with configuration B, where the illumination uniformity was significantly improved. This was demonstrated by a much rounder core in the x-ray pinhole camera images [compare Fig. 12(a) to Fig. 11(a)]. Adding the 20 spike beams did not further improve the roundness of the core emission. Figure 12 shows images using (b) no phase plates and (c) small spot phase plates in the 20 spike beams, respectively. Core distortions

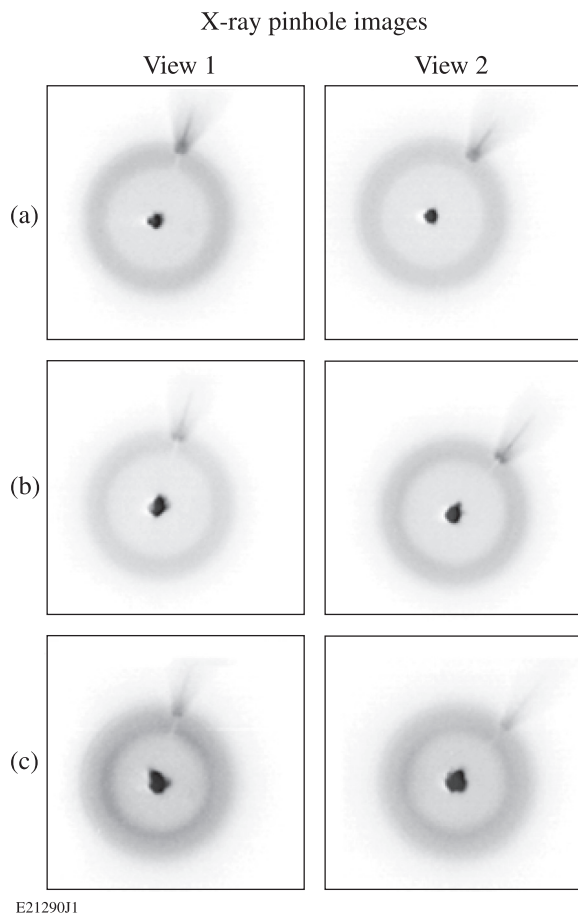


FIG. 12. Measured time-integrated x-ray pinhole images for configuration B. Two views from different directions are shown in each row. (a) The top row represents a 40-beam implosion, (b) the middle row a 40 + 20 implosion (no phase plates in the spike beams), and (c) the lower row a 40 + 20 implosion with phase plates in the spike beams.

are even slightly worse than in Fig. 12(a). A stronger x-ray emission was observed in Fig. 12(c) with phase plates. Figure 13 shows the (a) measured and (b) simulated neutron yields for these implosions. Implosions with repointed 40 drive beams produced neutron yields of $\sim 1.5 \times 10^9$ [solid line in Fig. 13(a)], which is a factor of ~ 6 higher than in the implosions where beams were pointed to target center. Adding the 20 spike beams, and, therefore, more energy on target, enhances the yield further by a factor of up to 2.3, with a trend of slightly lower yields at later spike onset. With 20 spike beams, the overall neutron yield is very similar to configuration A. The neutron yield shows no significant dependence on the spike intensity. A similar trend is observed in the predicted neutron yield from 1-D CHIC simulations [Fig. 13(b)]. There the enhancement is up to a factor of ~ 3.5 when adding the spike beams, slightly more than what was measured. Configuration B starts with a good illumination pattern in the 40 drive beams, but the 20 spike beams probably increased nonuniformities. This might explain why the yield increase is less than predicted. The yield over-clean (YOC) ratio, defined as the measured-to-predicted neutron number, is 3% to 5% for these experiments. The low YOC can be explained by a strong Rayleigh–Taylor instability growth during the deceleration phase in the low-velocity plastic-shell implosions and a substantial shell–fuel mixing that quenches fusion reactions.¹⁸

Figure 14 shows electron-temperature (top half) and pressure (bottom half) maps obtained from various 2-D CHIC simulations for configuration B. Hot electrons were not included in the simulations. This is probably justified for

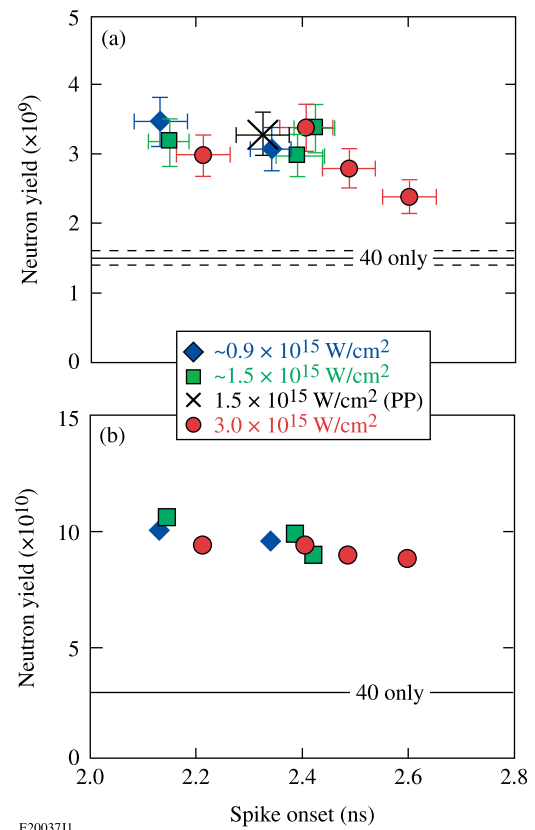


FIG. 13. (a) Measured and (b) 1-D-simulated neutron yields for configuration B.

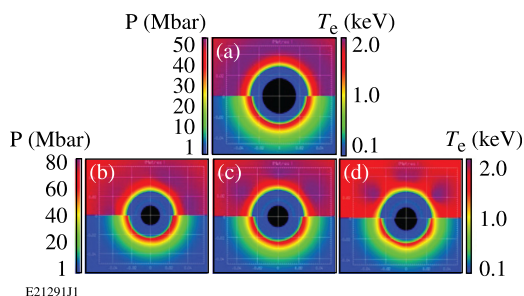


FIG. 14. Two-dimensional CHIC simulations. Electron temperature (top half) and pressure (bottom half): (a) without a spike at the end of the drive pulse (2.6 ns) and with a spike, 300 ps after the spike onset (2.9 ns) with (b) $SBI \sim 0.5 \times 10^{15} \text{ W/cm}^2$, (c) $SBI \sim 1 \times 10^{15} \text{ W/cm}^2$, and (d) $SBI \sim 2.5 \times 10^{15} \text{ W/cm}^2$. The temperature and pressure scales are the same for (b)–(d).

most of the shots in configuration B without phase plates since those shots are not affected much by hot electrons (see Fig. 15). Figure 14(a) shows the case without a spike pulse. The 40-beam illumination corresponds to that rendered in Fig. 2(c). In this case, the corona temperature and pressure are isotropic during the shell implosion, and the

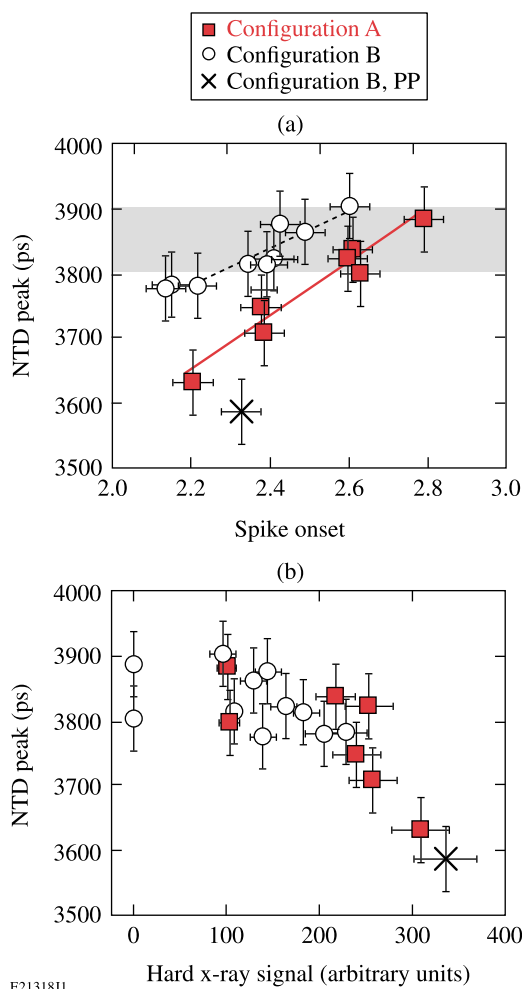


FIG. 15. Measured neutron bang time versus (a) the spike onset time and (b) the hard x-ray signal. The solid squares and open circles represent the measurements in configurations A and B, respectively, and the cross represents the measurement with phase plates in the spike beams in configuration B. The gray band in (a) denotes the range of measured bang times in 40-beam implosions.

shock pressure is about 50 Mbar at the end of the drive pulse ($t = 2.6 \text{ ns}$). Figures 14(b)–14(d) show 2-D simulations 300 ps after the spike onset for different focusing conditions of the spike beams (see Fig. 5), i.e., with different SBI. Some spike laser imprint in the corona is observed in the temperature map at high intensities, while with lower intensity, the temperature becomes more symmetric because of a better spatial overlap of the 20 spike beams. Independent of the spike intensity on target, however, the pressure remains symmetric with the same value of $\sim 75 \text{ Mbar}$. Some slight pressure modulations are observed at the highest intensity. The simulations show that the temperature in the conduction layer is fairly symmetric, which explains why the spike pressure keeps the same values in all the cases. For all focus conditions, the equivalent pressure can be estimated from the average spike intensity, which is $\langle I_{\text{spike}} \rangle \sim 0.5 \times 10^{15} \text{ W/cm}^2$. The total intensity on target is the sum of the spike intensity and the compression intensity ($I_{\text{comp}} = \sim 0.4 \times 10^{15} \text{ W/cm}^2$). For a laser absorption of about 70%, the absorbed intensity is $I_{\text{abs}} = \sim 0.7(I_{\text{comp}} + \langle I_{\text{spike}} \rangle) = \sim 0.6 \times 10^{15} \text{ W/cm}^2$, and the expected pressure is $\sim 80 \text{ Mbar}$ for this intensity from a simple scaling law model,³² in agreement with the simulated value. The 2-D simulations explain why for all SBI, the spike pressure remains constant, as does consequently the neutron yield. This argument applies only for the experiments with configuration B, while for configuration A, the neutron yields are dominated by the illumination nonuniformities and their mitigation by the spike beams.

The neutron temporal diagnostic²⁸ recorded the fusion reaction-rate history in most of the implosions, provided that the neutron yield was above $\sim 1 \times 10^9$. The signals are noisy and the peak of the measured neutron rate or “bang time” was obtained by fitting a Gaussian curve to the signals. The error in determining the bang time is estimated with $\sim 50 \text{ ps}$. The bang time is plotted in Fig. 15(a) versus spike onset. Bang times are earlier in configuration A for a given spike onset. The general trend for both data sets is that the bang time is later with a later onset of the spike pulse. The gray band marks the range of measured bang times from 40 drive beam implosions in configuration B. The solid line is a linear fit through the squares. The slope of this line is $\sim 1.6 \times$ larger than the slope of the dashed line, which is a linear fit through the circles. This indicates a stronger effect of the spike pulse in configuration A. However, the earliest bang time ($\sim 3.59 \text{ ns}$) was measured in one 40 + 20 shot with phase plates in the spike beams in configuration B. This is $\sim 200 \text{ ps}$ earlier than in the 40 drive beam implosions. Figure 15(b) shows that it is not so much the particular beam configuration that is important for the bang time; the amount of hot electrons that are generated (see Sec. VI) is more important. A clear correlation of the bang time with the measured hard x-ray signal is observed. An earlier bang time correlates with a higher x-ray signal indicating that the hot electrons affect the hydrodynamic implosion.

VI. HARD X-RAY MEASUREMENTS

The HXR detector provides information on the temperature of the electron distribution. The measured time-resolved

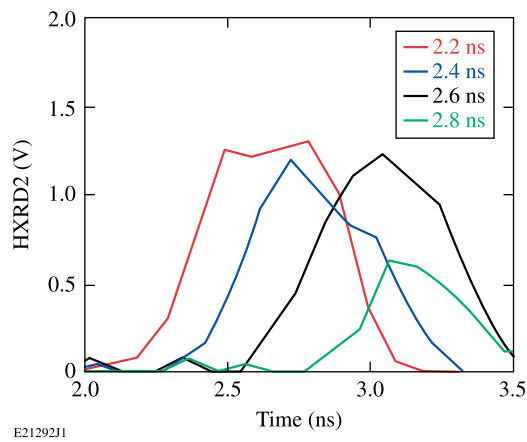


FIG. 16. Measured time-resolved hard x-ray pulses for energies >40 keV. The times in the legend indicate the onset of the spike pulse. The hard x-ray pulse is clearly correlated with the spike pulse, both in onset and duration.

hard x-ray pulse from the >40 -keV channel is shown in Fig. 16 for various spike-onset times. The hard x-ray pulse correlates with the spike laser pulse, both with respect to the onset and its duration. The hard x rays and, therefore, the hot electrons are predominantly produced by the high-intensity laser spike and are negligible when only the 40 low-intensity drive beams are used.

The hot-electron temperature for configuration A [Fig. 17(a)] was determined by fitting estimated values from the convolution of an exponentially decaying hard x-ray spectrum with the sensitivity of the different channels of the HXR detector to the three measured higher-energy channels.³⁰ The lowest-energy channel was excluded from the fit. A hot-electron-energy distribution with a temperature of ~ 30 keV was measured, independent of laser intensity and timing. Large-scale, collisional, 1-D particle-in-cell (PIC) simulations³³ for laser intensities of 10^{15} to 10^{16} W/cm² using very similar plasma parameters, reported hot-electron temperatures of ~ 25 keV, with the primary source for hot electrons being SRS. Remarkably, the simulations³³ predict a relatively low, constant hot-electron temperature that does not change with laser intensity, in agreement with the experimental observation.

Figure 17(b) shows the time-integrated hard x-ray yield of the >40 -keV channel. It is interesting to note that for implosions in configuration A, there is a clear correlation between the measured neutron signal (Fig. 10) and the hard x-ray signal [Fig. 17(b)], which suggests that the yield increase from adding the spike beams was partially due to hot electrons coupled into of the compressing target. It can be excluded that hard x rays interfered with the neutron-yield measurements because of proper shielding of the diagnostics and time-resolved measurements. Hard x rays were measured during the time of the spike pulse, while the neutron time-of-flight signal was measured much later in time. As mentioned before, the neutron signal is very sensitive to the condition of the target illumination. Adding the 20 spike beams in configuration A probably mitigated the nonuniformities, resulting in a much-higher ($\times 14$) neutron yield. This indicates that the spike beam's energy was coupled by

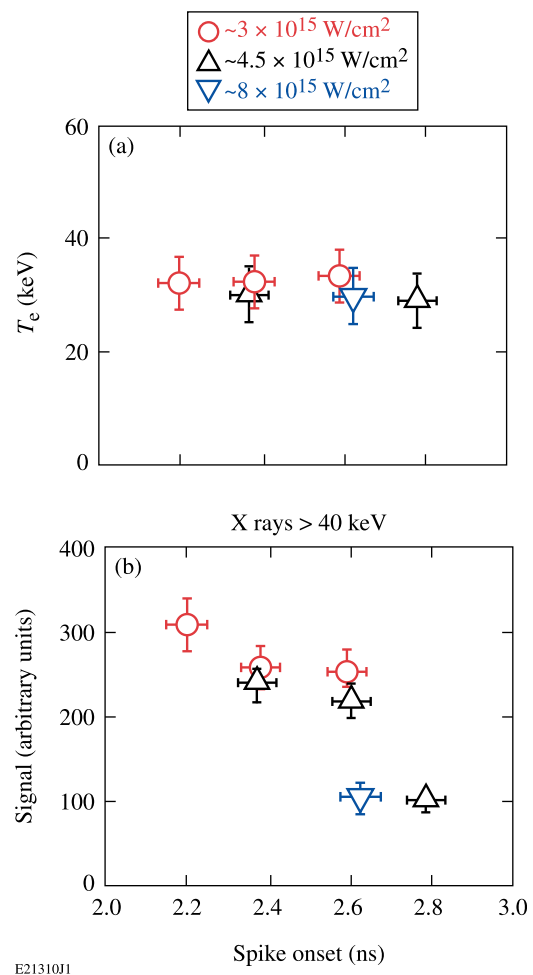


FIG. 17. (a) Inferred hot-electron temperature and (b) measured, time-integrated hard x ray signal >40 keV for configuration A.

inverse bremsstrahlung absorption and partially by hot electrons that slowed down in the dense shell.

Higher hard x-ray signals were measured for early spike onset, probably due to a longer temporal overlap between drive and spike pulse, which suggests that electron plasma waves seeded by the drive pulse were amplified by the high-intensity spike. More overlap provided a longer time period when the electron-plasma waves were driven; therefore, more hot electrons and higher hard x-ray signals were generated. The foci of the 20 spike beams did not overlap at the quarter-critical density (which is the location where the hot electrons are generated) for those measurements, so effects from overlapping beams³⁴ are not expected, and the hot-electron production was dominated by single beam interactions with the target. At 2.6 ns, there were three shots with different intensities. The hard x-ray signal decreased with higher intensity. Two causes might explain this effect: First, the backscatter losses increased from $\sim 10\%$ to $\sim 35\%$ (see below) with higher intensity, reducing the coupling efficiency of the spike beams. Second, since the SBI was varied through the focus size while holding the energy constant, a higher intensity corresponds to a smaller spot size. This affected the total number of generated hot electrons and the hard x-ray signal. The number of hot electrons is proportional to the plasma volume intercepted by the high-intensity

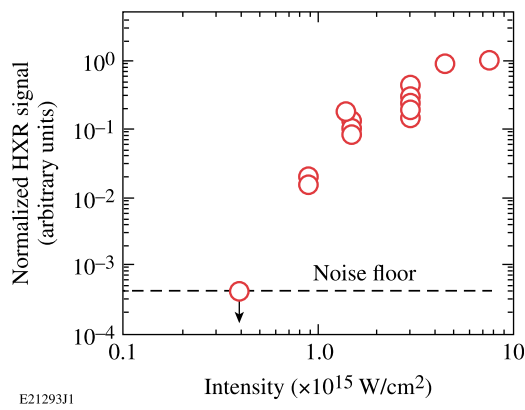


FIG. 18. Hard x-ray signal divided by the estimated laser-beam area at quarter-critical density as a function of SBI. The maximum signal was normalized to unity. Data from both configurations are plotted.

beams. When normalizing the measured hard x-ray signal by the estimated laser beam area at quarter-critical density, the yield actually increased with laser intensity (see Fig. 18). This shows that the hot-electron production per area increased with laser intensity, presumably because of a larger growth of laser-plasma instabilities. As in previous experiments performed under similar conditions,³⁴ the hard x-ray signal saturates at intensities above $\sim 2 \times 10^{15}$ W/cm².

Similar measurements were performed for beam configuration B (see Fig. 19). Here, the SBI was varied between 0.9×10^{15} and $\sim 3 \times 10^{15}$ W/cm². In contrast to the previous experiment, the foci of the spike beams were large enough at the lowest intensity, so that they partially overlapped [see Fig. 5(c)]. Not surprising, the lowest hard x-ray signal was measured for the lowest intensity. The inferred temperature was ~ 30 keV for all the shots without phase plates, independent of laser intensity and timing, which is very similar to the temperature in configuration A. A slightly higher temperature of ~ 40 keV was measured with phase plates, which also produced the highest hard x-ray signal for this beam configuration. Less backscattering (see Sec. VII) and less beam filamentation are expected with phase plates.³⁵ Spike beams that were not equipped with phase plates are susceptible to filamentation at plasma densities well below quarter critical density that might disrupt the beam significantly. With phase plates less beam disruption is expected that might have increased the average intensity at the quarter critical density compared to beams without phase plates. The TPD instability occurs close to the quarter-critical density. Only for this shot with phase plates, a measureable 3/2-harmonic signal³⁴ was present, which is a signature of TPD. The 3/2 signal was absent in all other shots without phase plates. The hotter electron distribution might, therefore, be due to some contribution from TPD, while the shots without phase plates were dominated by the SRS instability (see Sec. VII).

For beam configuration B, there is no clear correlation between the neutron signal [Fig. 13(a)] and hard x-ray signal [Fig. 19(b)]. This can be explained by the fact that in configuration B, a relatively uniform 40-beam implosion was distorted when the 20 spike beams were added. The 20 spike beams imposed a dodecahedron imprint pattern and seeded modulations [see Fig. 14] that increased the core deformation

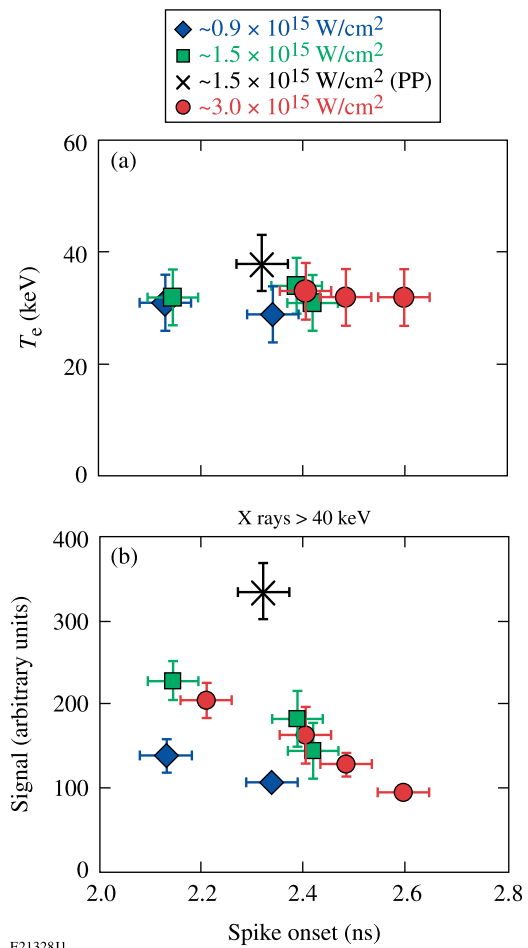
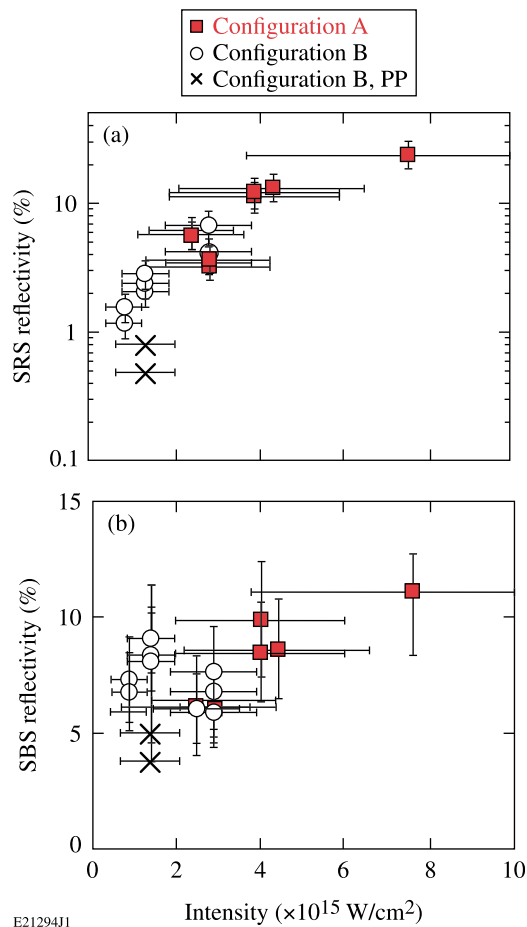


FIG. 19. (a) Inferred hot-electron temperature and (b) measured hard x-ray signal for configuration B.

at peak compression (Fig. 8). Larger core distortions were also observed in x-ray pinhole images when the spike beams were added [Figs. 12(b) and 12(c)]. This led to more Rayleigh–Taylor instability growth and reduced the neutron yields despite the additional energy that was coupled into the imploding shell. In general, adding laser energy from the spike beams should help to compress the shell more and boost the neutron yield, but there is a trade-off between more energy coupled into the target and more seeds for instabilities.

VII. BACKSCATTER MEASUREMENTS

The plasma reflectivity was measured for various laser intensities. Figure 20 shows the percentage of back-reflected light in the (a) SRS and (b) SBS channels of one of the spike beams. The SRS signal increased in intensity by more than a factor of ~ 10 to up to 24% and dominated the backscattering at the highest intensity, while SBS increased moderately from $\sim 5\%$ to 12%. A very low level of SRS backscattering ($\sim 0.5\%$) was measured at $\sim 1.5 \times 10^{15}$ W/cm² with phase plates in the spike beams. The simultaneously measured back-reflection through the neighboring drive-beam port, i.e., one of the 40 beam ports delivering the assembly pulse was low and remained about constant at the same level as in implosions without the 20 spike beams for all timings and

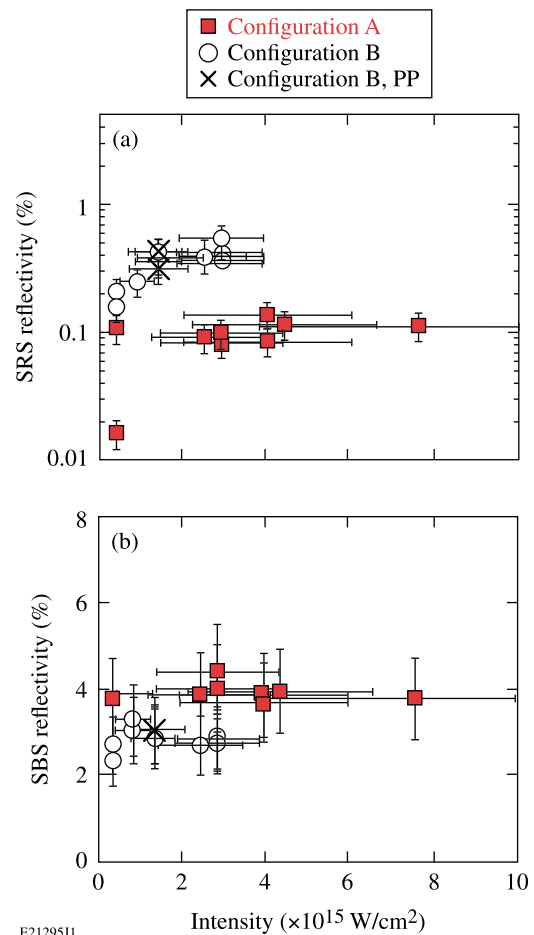


E21294J1

FIG. 20. Percentage of reflected laser light in a spike beam port by (a) SRS and (b) SBS as a function of SBI. Most of the high-intensity shots were done with configuration A denoted by the full squares. The open circles represent the repositioned beams (configuration B). The lowest reflectivity was measured with configuration B and phase plates (cross).

intensities (see Fig. 21). In the drive beam, SRS stayed below 1% and SBS in the 2% to 4% range.

This shows that the light from the spike beams was scattered back in a narrow cone and did not spill over into adjacent ports. It has been shown^{36,37} that smoothing the intensity distribution in the focal spot with spatial, temporal, and polarization smoothing schemes can substantially reduce the backscattering. This is attributed to a reduction of filamentation.³⁵ In most of the shots, no phase plates were used in the spike beams, which could explain the high levels of backscattering. The sum of SBS and SRS backscatter was lowest ($\sim 6\%$) with phase plates at $\text{SBI} \sim 1.5 \times 10^{15} \text{ W/cm}^2$ (sum of spike and drive intensity), while without phase plates, the reflectivity increased from $\sim 8\%$ at $\sim 0.9 \times 10^{15} \text{ W/cm}^2$ to $\sim 36\%$ at $\sim 8 \times 10^{15} \text{ W/cm}^2$. Most of the high-intensity shots were done with configuration A, but some shots were taken at $3 \times 10^{15} \text{ W/cm}^2$ with both beam configurations. The backscatter was the same within the measurement uncertainty. In contrast to the experiment, collisional PIC simulations³³ for similar plasma conditions predict that the calculated reflected laser energy should remain constant at $\sim 35\%$ when the laser intensity increases from $1 \times 10^{15} \text{ W/cm}^2$ to $8 \times 10^{15} \text{ W/cm}^2$. The simulations show that the fraction of energy absorbed by the col-



E21295J1

FIG. 21. Percentage of reflected laser light in a drive beam port by (a) SRS and (b) SBS as a function of SBI. See Fig. 20 for an explanation of the different symbols.

lisionless processes significantly increased with intensity, while the collisional absorption decreased proportionally.

A 2-D simulation with the radiation-hydrodynamics code *DRACO*³⁸ was performed to study the heating and the profile modification of the plasma under the interaction of a single high-intensity ($\sim 5 \times 10^{15} \text{ W/cm}^2$) spike beam with the imploding shell on the pole. No hot electrons were included in the simulations. The simulation shows the formation of a density depression in the underdense plasma and the steepening of the density profile at the critical density along the channel axis. Figure 22(a) shows axial density profiles for various times during the spike interaction. Figure 22(b) shows the density scale length at the critical density n_c (circles) and at $n_c/4$ (squares) along with the spike pulse's profile (dashed). Profile steepening at n_c occurs during the spike interaction, and the density scale length is reduced from $\sim 20 \mu\text{m}$ to $\sim 2 \mu\text{m}$. In contrast, the scale length at $n_c/4$ does not change significantly and remains $\sim 170 \mu\text{m}$ until the end of the spike pulse. As a result of this density profile modification, the spike pulse created a channel through the underdense plasma. Scattered light was guided by this channel and was dominantly reflected back into the incident beam with very little sidescattering. This is supported by the small amount of scatter in the drive beam (Fig. 21) and that

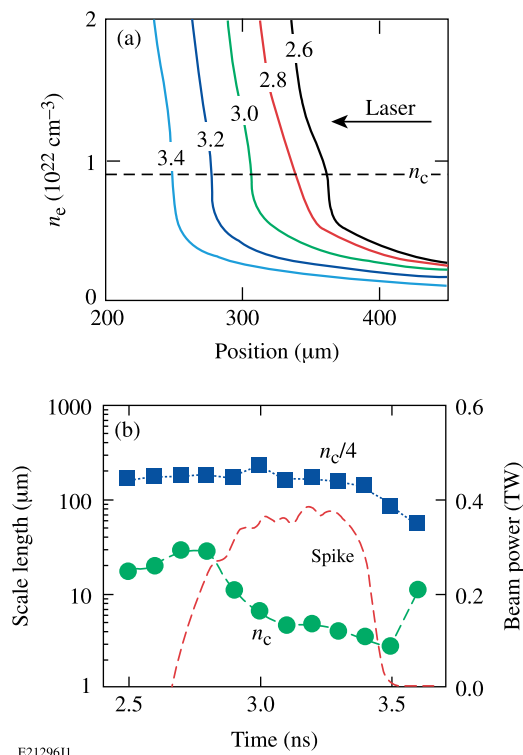


FIG. 22. (a) Density profiles from a 2-D hydrodynamic code *DRACO*³⁸ simulation along the channel axis of a high-intensity spike beam interacting with the imploding shell. The numbers indicate the time in nanoseconds. The critical density is marked by the dashed line. (b) Density scale length at critical (circles) and quarter-critical (squares) density. Profile steepening occurs when the spike pulse (dashed) interacts.

the near-backscatter diagnostic around the spike beam showed a negligible amount of sidescattering.

Time-resolved spectra of the SBS back-reflected light were recorded. Figure 23 shows two examples of the SBS signal for a medium- and high-intensity shot. The white curve represents the composite pulse shape of the drive and spike pulse. The SBS signal is only produced during the spike pulse. The frequency spectrum of the SBS light is affected by the plasmas temperature and by a Doppler shift with respect to the incident laser light. The amount of blue shift is given by $\omega - \omega_0 = 2k_0 c_s (M - 1) \sqrt{1 - n_e/n_c}$ (Ref. 39), where ω and ω_0 are the angular frequencies of the scattered and incident light, respectively, k_0 is the wave number of the incident light, c_s is the ion sound velocity, and M is the Mach number. Supersonic movement of the plasma region where SBS occurs will cause a blue shift of the SBS spectrum. The experiment shows that the blue shift is reduced with increasing laser intensity, indicating that SBS originates from plasma regions with lower flow velocities. A comparison with hydro simulations shows that lower flow velocities occur at higher plasma densities. The corresponding plasma density is indicated in the Fig. 23 by the ratio of electron density to n_c . For an intensity of $\sim 2.5 \times 10^{15} \text{ W/cm}^2$, the SBS active region was located at a plasma density of $\sim 0.03 n_c$. For $\sim 4.5 \times 10^{15} \text{ W/cm}^2$ (not shown), the peak emission shifted to $\sim 0.05 n_c$ with a weak SBS signal coming from up to $\sim n_c/4$ later in time. At the highest intensity [Fig. 23(b)], the SBS active region shifted up to ~ 0.1 to $0.2 n_c$

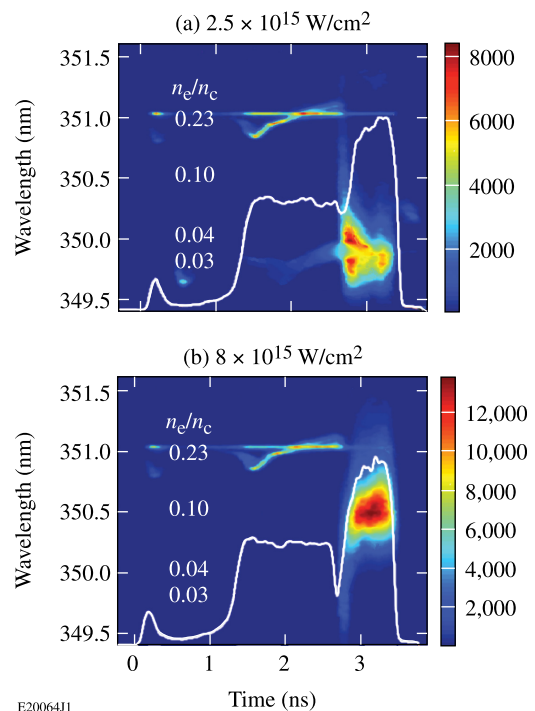


FIG. 23. Streaked SBS spectra for (a) medium ($\text{SBI} \sim 2.5 \times 10^{15} \text{ W/cm}^2$) and (b) high ($\text{SBI} \sim 8 \times 10^{15} \text{ W/cm}^2$) spike intensity. The numbers in the figures indicate the plasma density normalized to the critical density. The white curve is the composite pulse shape of the drive and spike pulses. This was in configuration A and no phase plates were used in the spike beams.

with clear indication of signal coming from above $n_c/4$. The laser-intensity threshold for SBS can be estimated with $I_{\text{SBS}} \approx (T_{\text{keV}}/L_v \lambda_\mu) \times (n_c/n_e) \times 7 \times 10^{15} \text{ W/cm}^2$ (Ref. 40), where T_{keV} , L_v , and λ_μ are the electron temperature in keV, the scale length of the Mach number profile in μm , and the laser wavelength in μm , respectively. The resulting threshold is $I_{\text{SBS}} \approx 5 \times 10^{14} \text{ W/cm}^2$ for the current plasma conditions and $n_e/n_c = 0.04$. The drive-pulse intensity is below the threshold, while the spike intensity is above the threshold.

The laser-intensity threshold for the TPD instability can be estimated from $I_{\text{TPD}} \approx (82 \times T_{\text{keV}}/L_\mu \lambda_\mu) \times 10^{14} \text{ W/cm}^2$ (Ref. 41), where L_μ is the density scale length in μm . For SRS, the threshold at around $\sim n_c/4$ is given by $I_{\text{SRS}} \approx (T_{\text{keV}}/L_\mu^{4/3} \lambda_\mu^{2/3}) \times 5 \times 10^{16} \text{ W/cm}^2$ (Ref. 40). *DRACO* simulations predict $T_{\text{keV}} \approx 1.8$, which results in $I_{\text{TPD}} \approx 2.5 \times 10^{14} \text{ W/cm}^2$ and $I_{\text{SRS}} \approx 2 \times 10^{14} \text{ W/cm}^2$ for the current plasma conditions. The thresholds are lower than the peak intensity in the drive beams, but no SRS or TPD signatures were measured with only the 40 drive beams.

With increasing intensity, a strong reduction of the optical emission at the half-harmonic ($\omega/2$) of the laser wavelength was observed. The $\omega/2$ signal decreased by more than two orders of magnitude in the applied intensity range. At the maximum intensity, the $\omega/2$ signal was below the detection threshold, indicating no significant contribution of TPD to the hot-electron production. This and the relatively low hot-electron temperature of $\sim 30 \text{ keV}$ supports the conjecture that SRS plays the dominant role in hot-electron production in these experiments. The strong reduction of $\omega/2$ with intensity, together with the observed shift of the SBS active

region to $\sim n_c/4$, might indicate that driven ion-acoustic waves at $\sim n_c/4$ play a role in the reduction of TPD.

VIII. CONCLUSIONS

Spherical shock-ignition experiments were performed on OMEGA by using a beam configuration that separates low-intensity compression beams and high-intensity spike beams. D₂-filled plastic shells were compressed on a low adiabat by 40 of the 60 OMEGA beams, and the remaining 20 spike beams were delayed and tightly focused onto the imploding shell to deliver a late shock. This paper studied the implosion performance with the new beam configuration and used the platform to measure hot-electron production and laser backscattering for laser intensities that are relevant for shock ignition. Two different beam-pointing configurations were used: one that uses the standard pointing to target center and another in which the beams were repointed to improve target illumination uniformity. Significant improvement in areal density and neutron yield and a rounder core in x-ray images were observed for the repointed beam configuration. Two-dimensional hydrodynamic simulations were performed for the repointed beam configuration that shows a modulation in the areal density at stagnation that is similar to the modulation observed in the experiment.

The coupling of high-intensity spike beam energy into the imploding capsule was studied. Implosions in the standard configuration show a correlation between the measured neutron yield and the hard x-ray signal, which suggests that the yield increase was partially due to hot electrons coupled into the compressing target. The spike beams mitigated the large beam illumination nonuniformities in this configuration, which led to the recovery of the neutron yield by a factor of ~ 14 . There are several indications that when the spike beams were equipped with phase plates, a stronger coupling of the spike beam energy into the imploding shell has been achieved. With phase plates the following observations were made: lower backscatter losses, stronger x-ray emission in the 2- to 7-keV and >20 -keV ranges, lower ρR , and an earlier bang time. This indicates that the higher coupling was achieved through increased thermal and hot-electron components.

Laser-plasma instabilities were studied for single-beam peak laser intensities of up to $\sim 8 \times 10^{15}$ W/cm², measuring backscattering of laser energy of up to 36% at the highest intensity. Hard x-ray measurements reveal a relatively low hot-electron temperature of ~ 30 keV, which is independent of intensity and spike onset time. With increasing laser intensity, the region where stimulated Brillouin scattering occurred shifted to higher densities. At the highest intensity, it occurred near and above the quarter-critical density. With higher intensity, the two-plasmon-decay instability was suppressed, and hot-electron production was dominated by stimulated Raman scattering.

These experiments measured a low hot-electron temperature, not too high backscatter losses, and a good coupling of spike beam energy into an imploding capsule at laser intensities of up to $\sim 8 \times 10^{15}$ W/cm², which is encouraging for the shock-ignition concept. A low hot-electron temperature

is beneficial since these electrons are stopped in the outer layer of the imploding target, augmenting the strong hydrodynamic shock. Further shock-ignition experiments are required, however, to study laser-plasma instabilities and hot-electron production at plasma conditions with longer density scale length and higher electron temperatures that are closer to those of an ignition design.

ACKNOWLEDGMENTS

This work was supported by the U.S. Department of Energy Office of Fusion Energy Sciences under Contract DE-FC02-04ER54789 and by the Office of Inertial Confinement Fusion under Cooperative Agreement No. DE-FC52-08NA28302, the University of Rochester, and the New York State Energy Research and Development Authority. The support of DOE does not constitute an endorsement by DOE of the views expressed in this article. This work was partially supported by the Aquitaine Region Council and the European Union's Seventh Framework Program: the HiPER Project #211737.

APPENDIX: BEAM POINTING AND FOCUSING

Tables I and II list the details of the beam pointing and focusing conditions for configurations A and B, respectively. The first column indicates to which group, drive (D) or spike (S), the beam belongs. Each beam is identified by a two digit number (second column) where the first digit indicates from which cluster the beam stems. The third and fourth columns in Table I give the nominal beam angles in the polar and the azimuthal direction, respectively. In configuration A, all beams were pointed to target center, which is indicated by the pointing location $R_p = 0$ mm (5th column). Accordingly, each beam was normally incident on the target surface (6th column). The third, fourth, and fifth columns in Table II give the spherical coordinates (r , Θ , Φ) of the beam pointing position. Note that most of the drive beams were repointed to a new position on an imaginary sphere with a radius that was equal to the initial target radius. Four out of the 40 drive beams were not repointed and aimed at the target center. The sixth column lists the angle of incidence of each beam with respect to the tangent target surface. The last three columns list the focusing lens positions for the three SBI cases. The lens position is given with respect to the target center. A negative number means that the focus was located in front of the target center, while for a positive number, the focus was behind the target when looked from the incident beam direction. In configuration B (Table II), the lens position of each spike beam was individually adjusted to compensate for the larger focal spot for oblique incident beams. The lens position was adjusted such that the intensity in each beam was the same. Assuming a round beam cross section, the lens position x was calculated by $x = x_0/\sqrt{\cos\alpha}$, where x_0 is the lens position for normal incidence and α is the angle of incidence of the beam. In shots where the spike beams were equipped with small spot phase plates (1.5×10^{15} W/cm²), a lens position of 0 mm was used for the spike beams.

TABLE I. Details of the beam pointing and focusing conditions for configuration A.

Beam	ID	Θ_B ($^\circ$)	Φ_B ($^\circ$)	R_P (mm)	α ($^\circ$)	8.0×10^{15} W/cm 2 LP (mm)	4.5×10^{15} W/cm 2 LP (mm)	3.0×10^{15} W/cm 2 LP (mm)
D	10	58.85	5.94	0	0.00	0.00	0.00	0.00
D	11	42.02	54.00	0	0.00	0.00	0.00	0.00
D	12	137.98	18.00	0	0.00	0.00	0.00	0.00
D	13	58.85	77.94	0	0.00	0.00	0.00	0.00
D	14	121.15	66.06	0	0.00	0.00	0.00	0.00
D	15	81.25	329.46	0	0.00	0.00	0.00	0.00
D	16	98.75	318.54	0	0.00	0.00	0.00	0.00
D	17	21.42	342.00	0	0.00	0.00	0.00	0.00
D	18	98.75	77.46	0	0.00	0.00	0.00	0.00
D	19	158.59	306.00	0	0.00	0.00	0.00	0.00
S	20	58.85	30.06	0	0.00	-0.30	0.37	0.77
S	21	121.15	329.94	0	0.00	-0.30	0.37	0.77
S	22	21.42	54.00	0	0.00	-0.30	0.37	0.77
S	23	121.15	41.94	0	0.00	-0.30	0.37	0.77
S	24	81.25	66.54	0	0.00	-0.30	0.37	0.77
S	25	158.59	90.00	0	0.00	-0.30	0.37	0.77
S	26	42.02	270.00	0	0.00	-0.30	0.37	0.77
S	27	98.75	30.54	0	0.00	-0.30	0.37	0.77
S	28	58.85	318.06	0	0.00	-0.30	0.37	0.77
S	29	137.98	306.00	0	0.00	-0.30	0.37	0.77
D	30	158.59	18.00	0	0.00	0.00	0.00	0.00
D	31	42.02	342.00	0	0.00	0.00	0.00	0.00
D	32	81.25	41.46	0	0.00	0.00	0.00	0.00
D	33	58.85	293.94	0	0.00	0.00	0.00	0.00
D	34	98.75	293.46	0	0.00	0.00	0.00	0.00
D	35	98.75	5.46	0	0.00	0.00	0.00	0.00
D	36	81.25	282.54	0	0.00	0.00	0.00	0.00
D	37	81.25	354.54	0	0.00	0.00	0.00	0.00
D	38	121.15	282.06	0	0.00	0.00	0.00	0.00
D	39	121.15	354.06	0	0.00	0.00	0.00	0.00
D	40	81.25	185.46	0	0.00	0.00	0.00	0.00
D	41	81.25	257.46	0	0.00	0.00	0.00	0.00
D	42	98.75	174.54	0	0.00	0.00	0.00	0.00
D	43	121.15	257.94	0	0.00	0.00	0.00	0.00
D	44	121.15	185.94	0	0.00	0.00	0.00	0.00
D	45	158.59	162.00	0	0.00	0.00	0.00	0.00
D	46	21.42	270.00	0	0.00	0.00	0.00	0.00
D	47	81.25	138.54	0	0.00	0.00	0.00	0.00
D	48	58.85	246.06	0	0.00	0.00	0.00	0.00
D	49	98.75	246.54	0	0.00	0.00	0.00	0.00
S	50	137.98	90.00	0	0.00	-0.30	0.37	0.77
S	51	121.15	210.06	0	0.00	-0.30	0.37	0.77
S	52	58.85	221.94	0	0.00	-0.30	0.37	0.77
S	53	98.75	149.46	0	0.00	-0.30	0.37	0.77
S	54	137.98	234.00	0	0.00	-0.30	0.37	0.77
S	55	42.02	198.00	0	0.00	-0.30	0.37	0.77
S	56	21.42	126.00	0	0.00	-0.30	0.37	0.77
S	57	121.15	138.06	0	0.00	-0.30	0.37	0.77
S	58	58.85	149.94	0	0.00	-0.30	0.37	0.77
S	59	81.25	113.46	0	0.00	-0.30	0.37	0.77
D	60	81.25	210.54	0	0.00	0.00	0.00	0.00
D	61	21.42	198.00	0	0.00	0.00	0.00	0.00
D	62	137.98	162.00	0	0.00	0.00	0.00	0.00
D	63	98.75	221.46	0	0.00	0.00	0.00	0.00
D	64	158.59	234.00	0	0.00	0.00	0.00	0.00
D	65	58.85	174.06	0	0.00	0.00	0.00	0.00
D	66	58.85	102.06	0	0.00	0.00	0.00	0.00
D	67	98.75	102.54	0	0.00	0.00	0.00	0.00
D	68	42.02	126.00	0	0.00	0.00	0.00	0.00
D	69	121.15	113.94	0	0.00	0.00	0.00	0.00

TABLE II Details of the beam pointing and focusing conditions for configuration B.

Beam	ID	R_P (mm)	Θ_P ($^\circ$)	Φ_P ($^\circ$)	α ($^\circ$)	3.0×10^{15} W/cm 2 LP (mm)	1.5×10^{15} W/cm 2 LP (mm)	0.9×10^{15} W/cm 2 LP (mm)
D	10	0.435	70.00	358.00	13.24	0.39	0.39	0.39
D	11	0.435	45.00	55.00	3.06	0.39	0.39	0.39
D	12	0.435	132.00	12.00	7.33	0.39	0.39	0.39
D	13	0.435	63.00	65.00	12.03	0.39	0.39	0.39
D	14	0.435	122.00	68.00	1.86	0.39	0.39	0.39
D	15	0	81.25	329.46	0	0.00	0.00	0.00
D	16	0	98.75	318.54	0	0.00	0.00	0.00
D	17	0.435	20.00	334.00	3.16	0.39	0.39	0.39
D	18	0.435	103.00	87.00	10.29	0.39	0.39	0.39
D	19	0	158.59	306.00	0	0.00	0.00	0.00
D	20	0.435	65.00	18.00	12.28	0.39	0.39	0.39
D	21	0	121.15	329.94	0	0.39	0.39	0.39
D	22	0.435	20.00	78.00	8.55	0.39	0.39	0.39
D	23	0.435	115.00	27.00	14.53	0.39	0.39	0.39
D	24	0.435	85.00	76.00	10.11	0.39	0.39	0.39
D	25	0.435	164.00	105.00	7.20	0.39	0.39	0.39
D	26	0.435	53.00	279.00	12.81	0.39	0.39	0.39
D	27	0.435	92.00	19.00	13.32	0.39	0.39	0.39
D	28	0.435	60.00	318.00	1.15	0.39	0.39	0.39
D	29	0	137.98	306.00	0	0.00	0.00	0.00
S	30	0.360	142.62	38.00	18.55	0.75	1.46	3.41
S	31	0.360	37.38	362.00	13.54	0.76	1.48	3.45
S	32	0.360	79.19	74.00	32.12	0.71	1.38	3.22
S	33	0.360	37.38	290.00	21.66	0.74	1.45	3.37
S	34	0.360	100.81	254.00	38.91	0.68	1.32	3.09
S	35	0.360	100.81	38.00	32.12	0.71	1.38	3.22
S	36	0.360	79.19	290.00	7.63	0.77	1.49	3.48
S	37	0.360	79.19	362.00	7.63	0.77	1.49	3.48
S	38	0.360	142.62	326.00	38.26	0.68	1.33	3.10
S	39	0.360	100.81	326.00	32.98	0.71	1.37	3.21
D	40	0.435	75.00	197.00	12.90	0.39	0.39	0.39
D	41	0.435	83.00	267.00	9.61	0.39	0.39	0.39
D	42	0.435	101.00	181.00	6.75	0.39	0.39	0.39
D	43	0.435	120.00	264.00	5.34	0.39	0.39	0.39
D	44	0.435	120.00	184.00	2.03	0.39	0.39	0.39
D	45	0.435	164.00	159.00	5.50	0.39	0.39	0.39
D	46	0.435	20.00	276.00	2.55	0.39	0.39	0.39
D	47	0.435	76.00	137.00	5.46	0.39	0.39	0.39
D	48	0.435	63.00	255.00	8.84	0.39	0.39	0.39
D	49	0.435	99.00	254.00	7.37	0.39	0.39	0.39
D	50	0.435	139.00	94.00	2.84	0.39	0.39	0.39
D	51	0.435	113.00	213.00	8.56	0.39	0.39	0.39
D	52	0.435	58.00	215.00	5.97	0.39	0.39	0.39
D	53	0.435	94.00	139.00	11.43	0.39	0.39	0.39
D	54	0.435	135.00	238.00	4.06	0.39	0.39	0.39
D	55	0.435	46.00	186.00	9.23	0.39	0.39	0.39
D	56	0.435	25.00	139.00	6.23	0.39	0.39	0.39
D	57	0.435	129.00	139.00	7.89	0.39	0.39	0.39
D	58	0.435	49.00	151.00	9.89	0.39	0.39	0.39
D	59	0.435	82.00	109.00	4.47	0.39	0.39	0.39
S	60	0.360	79.19	218.00	7.63	0.77	1.49	3.48
S	61	0.360	37.38	218.00	18.55	0.75	1.46	3.41
S	62	0.360	142.62	182.00	13.54	0.76	1.48	3.45
S	63	0.360	100.81	182.00	38.91	0.68	1.32	3.09
S	64	0.360	142.62	254.00	18.55	0.75	1.46	3.41
S	65	0.360	79.19	146.00	32.98	0.71	1.37	3.21
S	66	0.360	37.38	74.00	29.60	0.72	1.40	3.26
S	67	0.360	100.81	110.00	7.63	0.77	1.49	3.48
S	68	0.360	37.38	146.00	13.54	0.76	1.48	3.45
S	69	0.360	142.62	110.00	21.66	0.74	1.45	3.37

- ¹R. Betti, C. D. Zhou, K. S. Anderson, L. J. Perkins, W. Theobald, and A. A. Solodov, *Phys. Rev. Lett.* **98**, 155001 (2007).
- ²R. L. McCrory, D. D. Meyerhofer, R. Betti, R. S. Craxton, J. A. Delettrez, D. H. Edgell, V. Yu. Glebov, V. N. Goncharov, D. R. Harding, D. W. Jacobs-Perkins, J. P. Knauer, F. J. Marshall, P. W. McKenty, P. B. Radha, S. P. Regan, T. C. Sangster, W. Seka, R. W. Short, S. Skupsky, V. A. Smalyuk, J. M. Soures, C. Stoeckl, B. Yaakobi, D. Shvarts, J. A. Frenje, C. K. Li, R. D. Petrasso, and F. H. Séguin, *Phys. Plasmas* **15**, 055503 (2008).
- ³J. D. Lindl, *Inertial Confinement Fusion: The Quest for Ignition and Energy Gain Using Indirect Drive* (Springer-Verlag, New York, 1998).
- ⁴V. A. Shcherbakov, *Sov. J. Plasma Phys.* **9**, 240 (1983).
- ⁵R. Betti and C. Zhou, *Phys. Plasmas* **12**, 110702 (2005).
- ⁶X. Ribeyre, Ph. Nicolaï, G. Schurtz, M. Olazabal-Loumé, J. Briel, P. H. Maire, J. Feugeas, L. Hallo, and V. T. Tikhonchuk, *Plasma Phys. Controlled Fusion* **50**, 025007 (2008).
- ⁷A. J. Schmitt, J. W. Bates, S. P. Obenschain, S. T. Zalesak, D. E. Fyfe, and R. Betti, *Fusion Sci. Technol.* **56**, 377 (2009).
- ⁸X. Ribeyre, G. Schurtz, M. Lafon, S. Galera, and S. Weber, *Plasma Phys. Controlled Fusion* **51**, 015013 (2009).
- ⁹E. I. Moses, R. N. Boyd, B. A. Remington, C. J. Keane, and R. Al-Ayat, *Phys. Plasmas* **16**, 041006 (2009).
- ¹⁰L. J. Perkins, R. Betti, K. N. LaFortune, and W. H. Williams, *Phys. Rev. Lett.* **103**, 045004 (2009).
- ¹¹M. Dunne, *Nat. Phys.* **2**, 2 (2006); See <http://www.hiper-laser.org/index.html> for HiPER, accessed 7 May 2012.
- ¹²W. L. Kruer, *The Physics of Laser-Plasma Interactions*, *Frontiers in Physics*, Vol. 73, edited by D. Pines (Addison-Wesley, Redwood City, CA, 1988).
- ¹³R. Betti, W. Theobald, C. D. Zhou, K. S. Anderson, P. W. McKenty, S. Skupsky, D. Shvarts, V. N. Goncharov, J. A. Delettrez, P. B. Radha, T. C. Sangster, C. Stoeckl, and D. D. Meyerhofer, *J. Phys.: Conf. Ser.* **112**, 022024 (2008).
- ¹⁴J. Delettrez, R. Epstein, M. C. Richardson, P. A. Jaanimagi, and B. L. Henke, *Phys. Rev. A* **36**, 3926 (1987); M. C. Richardson, P. W. McKenty, F. J. Marshall, C. P. Verdon, J. M. Soures, R. L. McCrory, O. Barnouin, R. S. Craxton, J. Delettrez, R. L. Hutchison, P. A. Jaanimagi, R. Keck, T. Kessler, H. Kim, S. A. Letzring, D. M. Roback, W. Seka, S. Skupsky, B. Yaakobi, S. M. Lane, and S. Prussin, in *Laser Interaction and Related Plasma Phenomena*, edited by H. Hora and G. H. Miley (Plenum, New York, 1986), Vol. 7, p. 421.
- ¹⁵T. R. Boehly, D. L. Brown, R. S. Craxton, R. L. Keck, J. P. Knauer, J. H. Kelly, T. J. Kessler, S. A. Kumpan, S. J. Loucks, S. A. Letzring, F. J. Marshall, R. L. McCrory, S. F. B. Morse, W. Seka, J. M. Soures, and C. P. Verdon, *Opt. Commun.* **133**, 495 (1997).
- ¹⁶W. Theobald, K. S. Anderson, R. Betti, R. S. Craxton, J. A. Delettrez, J. A. Frenje, V. Yu. Glebov, O. V. Gotchev, J. H. Kelly, C. K. Li, A. J. Mackinnon, F. J. Marshall, R. L. McCrory, D. D. Meyerhofer, J. F. Myatt, P. A. Norreys, P. M. Nilson, P. K. Patel, R. D. Petrasso, P. B. Radha, C. Ren, T. C. Sangster, W. Seka, V. A. Smalyuk, A. A. Solodov, R. B. Stephens, C. Stoeckl, and B. Yaakobi, *Plasma Phys. Controlled Fusion* **51**, 124052 (2009).
- ¹⁷R. S. Craxton, L. Tucker, T. Mo, K. S. Anderson, R. Betti, L. J. Perkins, G. P. Schurtz, X. Ribeyre, and C. A. Casner, *Bull. Am. Phys. Soc.* **55**, 26 (2010).
- ¹⁸W. Theobald, R. Betti, C. Stoeckl, K. S. Anderson, J. A. Delettrez, V. Yu. Glebov, V. N. Goncharov, F. J. Marshall, D. N. Maywar, R. L. McCrory, D. D. Meyerhofer, P. B. Radha, T. C. Sangster, W. Seka, D. Shvarts, V. A. Smalyuk, A. A. Solodov, B. Yaakobi, C. D. Zhou, J. A. Frenje, C. K. Li, F. H. Séguin, R. D. Petrasso, and L. J. Perkins, *Phys. Plasmas* **15**, 056306 (2008).
- ¹⁹F. J. Marshall, J. A. Delettrez, R. Epstein, R. Forties, R. L. Keck, J. H. Kelly, P. W. McKenty, S. P. Regan, and L. J. Waxer, *Phys. Plasmas* **11**, 251 (2004).
- ²⁰Y. Lin, T. J. Kessler, and G. N. Lawrence, *Opt. Lett.* **21**, 1703 (1996).
- ²¹T. R. Boehly, V. A. Smalyuk, D. D. Meyerhofer, J. P. Knauer, D. K. Bradley, R. S. Craxton, M. J. Guardalben, S. Skupsky, and T. J. Kessler, *J. Appl. Phys.* **85**, 3444 (1999).
- ²²P.-H. Maire, R. Abgrall, J. Breil, and J. Ovadia, *SIAM J. Sci. Comput.* **29**, 1781 (2007).
- ²³S. Pollaine and S. Hatchett, *Nucl. Fusion* **44**, 117 (2004).
- ²⁴S. P. Regan, T. C. Sangster, D. D. Meyerhofer, W. Seka, R. Epstein, S. J. Loucks, R. L. McCrory, C. Stoeckl, V. Yu. Glebov, O. S. Jones, D. A. Callahan, P. A. Amendt, N. B. Meezan, L. J. Suter, M. D. Rosen, O. L. Landen, E. L. DeWald, S. H. Glenzer, C. Sorce, S. Dixit, R. E. Turner, and B. MacGowan, *J. Phys.: Conf. Ser.* **112**, 022077 (2008).
- ²⁵C. D. Zhou, W. Theobald, R. Betti, P. B. Radha, V. A. Smalyuk, D. Shvarts, V. Yu. Glebov, C. Stoeckl, K. S. Anderson, D. D. Meyerhofer, T. C. Sangster, C. K. Li, R. D. Petrasso, J. A. Frenje, and F. H. Séguin, *Phys. Rev. Lett.* **98**, 025004 (2007).
- ²⁶F. J. Marshall, T. Ohki, D. McInnis, Z. Ninkov, and J. Carbone, *Rev. Sci. Instrum.* **72**, 713 (2001).
- ²⁷V. Yu. Glebov, D. D. Meyerhofer, C. Stoeckl, and J. D. Zuegel, *Rev. Sci. Instrum.* **72**, 824 (2001).
- ²⁸R. A. Lerche, D. W. Phillion, and G. L. Tietbohl, *Rev. Sci. Instrum.* **66**, 933 (1995).
- ²⁹W. Seka, D. H. Edgell, J. P. Knauer, J. F. Myatt, A. V. Maximov, R. W. Short, T. C. Sangster, C. Stoeckl, R. E. Bahr, R. S. Craxton, J. A. Delettrez, V. N. Goncharov, I. V. Igumenshchev, and D. Shvarts, *Phys. Plasmas* **15**, 056312 (2008).
- ³⁰C. Stoeckl, V. Yu. Glebov, D. D. Meyerhofer, W. Seka, B. Yaakobi, R. P. J. Town, and J. D. Zuegel, *Rev. Sci. Instrum.* **72**, 1197 (2001).
- ³¹F. H. Séguin, J. A. Frenje, C. K. Li, D. G. Hicks, S. Kurebayashi, J. R. Rygg, B.-E. Schwartz, R. D. Petrasso, S. Roberts, J. M. Soures, D. D. Meyerhofer, T. C. Sangster, J. P. Knauer, C. Sorce, V. Yu. Glebov, C. Stoeckl, T. W. Phillips, R. J. Leeper, K. Fletcher, and S. Padalino, *Rev. Sci. Instrum.* **74**, 975 (2003).
- ³²S. Atzeni and J. Meyer-ter-Vehn, *The Physics of Inertial Fusion: Beam Plasma Interaction, Hydrodynamics, Hot Dense Matter*, *International Series of Monographs on Physics* (Clarendon, Oxford, 2004), p. 225.
- ³³O. Klimo, V. T. Tikhonchuk, X. Ribeyre, G. Schurtz, C. Riconda, S. Weber, and J. Limpouch, *Phys. Plasmas* **18**, 082709 (2011).
- ³⁴C. Stoeckl, R. E. Bahr, B. Yaakobi, W. Seka, S. P. Regan, R. S. Craxton, J. A. Delettrez, R. W. Short, J. Myatt, A. V. Maximov, and H. Baldis, *Phys. Rev. Lett.* **90**, 235002 (2003).
- ³⁵C. Labaune, S. Baton, T. Jalinaud, H. A. Baldis, and D. Pesme, *Phys. Fluids B* **4**, 2224 (1992).
- ³⁶B. J. MacGowan, B. B. Afeyan, C. A. Back, R. L. Berger, G. Bonnaud, M. Casanova, B. I. Cohen, D. E. Desenne, D. F. DuBois, A. G. Dulieu, K. G. Estabrook, J. C. Fernández, S. H. Glenzer, D. E. Hinkel, T. B. Kaiser, D. H. Kalantar, B. I. Kauffman, R. K. Kirkwood, W. L. Kruer, A. B. Langdon, B. F. Lasinski, D. S. Montgomery, J. D. Moody, D. H. Munro, L. V. Powers, H. A. Rose, C. Rousseaux, R. E. Turner, B. H. Wilde, S. C. Wilks, and E. A. Williams, *Phys. Plasmas* **3**, 2029 (1996).
- ³⁷J. D. Moody, B. J. MacGowan, J. E. Rothenberg, R. L. Berger, L. Divol, S. H. Glenzer, R. K. Kirkwood, E. A. Williams, and P. E. Young, *Phys. Rev. Lett.* **86**, 2810 (2001).
- ³⁸P. B. Radha, T. J. B. Collins, J. A. Delettrez, Y. Elbaz, R. Epstein, V. Yu. Glebov, V. N. Goncharov, R. L. Keck, J. P. Knauer, J. A. Marozas, F. J. Marshall, R. L. McCrory, P. W. McKenty, D. D. Meyerhofer, S. P. Regan, T. C. Sangster, W. Seka, D. Shvarts, S. Skupsky, Y. Srebro, and C. Stoeckl, *Phys. Plasmas* **12**, 056307 (2005).
- ³⁹T. P. Hughes, in *Laser-Plasma Interactions*, edited by R. A. Cairns and J. Sanderson (SUSSP, Edinburgh, 1980), p. 44.
- ⁴⁰H. A. Baldis, E. M. Campbell, and W. L. Kruer, in *Handbook of Plasma Physics*, edited by A. Rubenchik and S. Witkowski, *Physics of Laser Plasma*, edited by M. N. Rosenbluth and R. Z. Sagdeev (North-Holland, Amsterdam, 1991), Vol. 3, p. 377.
- ⁴¹A. Simon, R. W. Short, E. A. Williams, and T. Dewandre, *Phys. Fluids* **26**, 3107 (1983).